JOURNAL OF TURBULENCE, 2016
VOL. 17, NO. 12, 1087–1111
http://dx.doi.org/10.1080/14685248.2016.1223846

Taylor & Francis
Taylor & Francis Group

On the mixing models for stratified flows subjected to concomitant stable and unstable stratifications

Duo Xu and Jun Chen

School of Mechanical Engineering, Purdue University, West Lafayette, IN, USA

ABSTRACT

The concurrence of stable and unstable stratification in stratified flows leads to dramatically different features of turbulent mixing. This unique flow is experimentally studied by introducing a horizontal jet of dense fluid into a pool of light fluid. The buoyancy flux from simultaneous velocity–density measurements is an indicator for competition between a stabilising mechanism and another destabilising mechanism. The difference of mixing efficiency, quantified by flux Richardson number Ri_f, between the (un)stable stratification is mainly contributed by the large-scale mixing. The behaviour of Ri_f can be modelled by the gradient Richardson number Ri_g linearly in the low-Ri case and nonlinearly in the high-Ri case (especially in a region where the counter-gradient flux emerges). The turbulent diapycnal diffusivity, quantifying the combined effect of reversible and irreversible mixing processes, increases as the buoyancy Reynolds number Re_b increases only when Re_b is large. The irreversible mixing diffusivity, which quantifies the sole irreversible mixing process, increases linearly as the turbulent Péclet number with the data points from the (un)stable stratification overlapped. The turbulent Prandtl number approaches 0.75 as Ri_g approaches zero, but does not show clear dependence on Ri_g in the examined regime.

ARTICLE HISTORY
Received 21 March 2016
Accepted 3 August 2016

KEYWORDS
Turbulent mixing; mixing modelling

1. Introduction

The interaction of stratification and turbulence is frequently observed in a variety of flows. Surface wind and heat advection at the air–sea interface drive the upper mixing layer of ocean into stably stratified oceanic pycnocline. The presence of buoyancy effect resulted from density stratification influences mixing and dispersion of pollutants and nutrients. In particular, it influences the heat and salt transports in Meridional Overturning Circulation whose abnormal changes may result in abrupt climate change.[e.g., 1,2] Similar phenomenon also exists at a relatively small scale in contaminant spread inside an airline cabin and all indoor environment where the conditioned air and return air are managed by HVAC systems.[e.g., 3] The interaction induces mixing the core fluid with the ambient fluid at a wide range of scales. The currently available numerical tools are inadequate to resolve all the spatial and temporal scales, so they rely on specific parameterisation or closure models,

CONTACT Jun Chen junchen@purdue.edu

which need to accurately represent the mixing physics. Particular interest is on quantifying the mixing efficiency under different stratification and turbulence levels.

The interaction of turbulence and stratification in stratified flows is described by the transport equation of turbulent kinetic energy (TKE), with the Boussinesq approximation [4]:

$$\langle u_j \rangle \frac{\partial k}{\partial x_j} + \frac{\partial T_j}{\partial x_j} = \mathcal{P} - \mathcal{B} - \epsilon, \tag{1}$$

where $k \equiv \langle u_i' u_i' \rangle / 2$ represents TKE and $T_j \equiv \langle u_j' u_i' u_i' \rangle / 2 + \langle u_j' p \rangle / \rho_s - 2\nu \langle u_i' s_{ij} \rangle$ a transport term. Here, $\langle \cdot \rangle$ and $(\cdot)'$ denote the averaging term and the corresponding fluctuation term, respectively, in Reynolds decomposition. (The velocity and scalar fields can thus be decomposed: $u_i(\mathbf{x}, t) = \langle u_i \rangle(\mathbf{x}) + u_i'(\mathbf{x}, t)$ and $\theta(\mathbf{x}, t) = \langle \theta \rangle(\mathbf{x}) + \theta'(\mathbf{x}, t)$, where $\theta(\mathbf{x}, t) \equiv \Delta\rho(\mathbf{x}, t)/\delta\rho_o$ is the non-dimensional density difference, $\Delta\rho$ the density difference and $\delta\rho_o$ the initial density difference.) In Equation (1), the turbulence production,

$$\mathcal{P} \equiv -\langle u_i' u_j' \rangle S_{ij}, \tag{2}$$

describes the production of TKE due to the gradients of mean velocity, where $S_{ij} = 0.5(\partial \langle u_i \rangle / \partial x_j + \partial \langle u_j \rangle / \partial x_i)$ is the strain rate tensor. The buoyancy flux,

$$\mathcal{B} \equiv g' \langle \theta' u_3' \rangle, \tag{3}$$

quantifies the production or consumption of TKE via mixing, where $g' \equiv g\delta\rho_o/\rho_s$ is the reduced gravity. The dissipation rate of TKE,

$$\epsilon = \nu \left\langle \frac{\partial u_i'}{\partial x_j} \frac{\partial u_i'}{\partial x_j} + \frac{\partial u_i'}{\partial x_j} \frac{\partial u_j'}{\partial x_i} \right\rangle, \tag{4}$$

describes the consumption of TKE by viscous process. Furthermore, the flux Richardson number,

$$Ri_f = \mathcal{B}/\mathcal{P}, \tag{5}$$

is referred to the mixing efficiency.[5–7]

To describe Ri_f, the eddy-viscosity–diffusivity approximations are usually employed to relate the turbulent momentum flux $\langle u_i' u_j' \rangle$ and scalar flux $\langle \theta' u_i' \rangle$ with the mean velocity gradients $\partial \langle u_i \rangle / \partial x_j$ and mean scalar gradients $\partial \langle \theta \rangle / \partial x_i$. As a result, Ri_f may be modelled by a gradient Richardson number

$$Ri_g = N^2/S^2, \tag{6}$$

where $N = \sqrt{(g/\rho_s)|\partial \langle \rho \rangle / \partial x_3|}$ is Brunt–Väisälä frequency (x_3 is anti-parallel to the gravitational direction) and $S = \sqrt{(\partial \langle u_1 \rangle / \partial x_3)^2 + (\partial \langle u_2 \rangle / \partial x_3)^2}$ is the mean shear rate.

The first $Ri_f - Ri_g$ relationship was proposed by assuming local thermodynamic equilibrium and neglecting the mean advection of flow.[8] By considering the convective effect, a second-moment $Ri_f - Ri_g$ model (Mellor–Yamada model) was later introduced by adopting

a low order of 'energy redistribution' hypothesis and a simple version of turbulent diffusivity model to achieve an optimal computational load without excessive loss of accuracy.[9] An improved version of the Mellor–Yamada model was developed for large eddy simulation (LES) of stably stratified and convective planetary boundary layers.[10] Other theoretical attempts for developing similar closure models were also reported, such as one-point model.[11] In addition to these theoretical attempts, the $Ri_f - Ri_g$ relationship has also been investigated by laboratory experiments,[12–14] numerical simulations,[6] and field measurement of either atmospheric boundary layer [15] or weakly stratified upper ocean in the North Atlantic.[16] The failure of a universal $Ri_f - Ri_g$ relationship from many studies, however, recently raises an argument that whether Ri_g alone is adequate to model the behaviour of Ri_f. It consequently gives rise to the modelling of Ri_f with a different parameter or multiple parameters. For example, a local buoyancy Reynolds number $Re_b = \epsilon/(\nu N^2)$ was introduced to parameterise Ri_f together with Ri_g.[17]

Another keen interest is on quantifying the mixing across isopycnal interfaces. This diapycnal mixing, usually indicated by the turbulent diapycnal diffusivity κ_θ, governs the heat and nutrient transfers across pycnocline or thermocline [18] and influences the predictions of global climate change.[19] κ_θ is associated with Re_b.[20,21] For instance, three regimes of mixing with Re_b were identified [20]: (i) the diffusive regime ($Re_b \sim 1$) where stratification is strong and κ_θ is of the same order as molecular diffusivity; (ii) the intermediate regime ($10 \lesssim Re_b \lesssim 100$) where κ_θ increases linearly with Re_b; and (iii) the energetic regime ($Re_b \gtrsim 100$) where stratification is weak and κ_θ increases more slowly. This parameterisation of κ_θ using Re_b has been recently questioned,[22,23] by arguing that κ_θ should be independent of molecular diffusivity κ, especially at high Reynolds number, but Re_b does not satisfy this independence. In the studies, the contributions of reversible and irreversible mixing processes were suggested to be considered separately, and the irreversible turbulent diapycnal diffusivity κ_ρ was introduced and can be modelled by a turbulent Péclet number

$$Pe_t = \frac{L_E^2}{\kappa T_L}, \tag{7}$$

with the Ellison overturning length scale $L_E = \sqrt{\langle\theta'^2\rangle}/|\partial\langle\theta\rangle/\partial x_3|$ and turbulence decay time scale $T_L = k/\epsilon$. This model was investigated using one-dimensional (1D) simulation of homogeneously sheared stratified turbulence and the improperness of modelling κ_θ by Re_b was later confirmed in simulations.[24] A similar approach (to separate the irreversible and reversible mixing) was applied to parameterise the vertical momentum eddy viscosity κ_m and the turbulent Prandtl number $Pr_t = \kappa_m/\kappa_\theta$.[25] (Before this study, Pr_t was often modelled by Ri_g [26–28] without distinguishing the irreversible and reversible mixing processes.) The argument also focuses on suitability of the Pr_t model to neutrally stratified flows (no stratification case, denoted by Pr_{t0}), which tests whether the modelling is physically based and whether it is applicable to both the passive scalar and active scalar cases. For example, $0.5 < Pr_{t0} < 1.0$ for neutrally stratified flows was suggested [29] and $Pr_{t0} = 0.7$ was obtained in the analytical derivation of the simplified TKE transport equation and later examined in DNS data of homogeneous stably stratified turbulence.[25].

Extensive experimental efforts have been put on understanding the mixing in stratified flows by in-situ measurements and laboratory experiments. A significant amount of in-situ data of oceanic flows have been collected by research vessels or float buoys loaded with

sensors.[e.g., 30,31] These valuable measurements are limited by their high cost, technical difficulty for achieving ideal spatial resolution, as well as the uncontrollable variations of flow conditions. The laboratory studies, on the other hand, are of well controlled flow conditions, but the ranges of length and time scales are far less than the ones in oceanic flows. As a result, most of the laboratory generated stratified flows have smaller Reynolds number at the order of hundreds or thousands. In addition, in a perspective of general stratified flows (e.g., in engineering applications), the numbered available measurement techniques present another challenge for experiment studies. Recent laboratory experiments investigated the mixing and the dynamics of stratified flows using flow visualisation (with colour dye) and/or point-wise measurement technique, e.g., laser Doppler velocimetry (LDV) [32–34] or planar laser-induced fluorescence (PLIF),[35–37] or a combined PLIF–particle image velocimetry (PIV) technique for simultaneously measuring scalar-velocity fields.[38–40] These data-sets lead to new perspectives of flow physics mostly in a setting of stably stratified flows, due to rich information collected: high-resolution data, simultaneous velocity-scalar fields, detailed turbulent energetics, availability of analysing velocity/scalar gradients, etc.

Nevertheless, stable and unstable stratification mechanisms often coexist or change from one to another, because of the effect of geophysical topography, periodic change of solar radiation, etc. One example is the development of alternating zonal jets in oceanic background stratification (see Ref.[41] and therein references), which affects the transport of heat, momentum and tracers. In addition, although the stable stratification exists in a global or statistical manner, local unstable stratification often emerges irregularly, to affect the flow characteristics. Unfortunately, the coexistent stable–unstable stratification has not attracted attentions (no study is yet on it to our best knowledge). More importantly, the mixing parameterisations/models were developed under the stable stratification circumstance, but extended to general stratified flows without discerning their performances in stable and unstable stratification regions. Whether such models are in a unifying framework in stable–unstable stratification flows are unknown. Characterising mixing dynamics under the unique concomitant stable and unstable stratification consequently motivates this laboratory experimental study.

In this paper, we report an investigation of mixing dynamics by analysing an experimental data-set collected from a horizontally induced stratified jet. The orthogonality of the directions of the initial momentum and the buoyancy introduces separated coexistent stable and unstable stratification regions. The high spatial resolution velocity–density data are used to examine the physics for modelling Ri_f, κ_θ and Pr_t. The paper is structured as follows. The experimental data-set is introduced in Section 2. Section 3 presents the methods of estimating the turbulent energetics using the experimental data. Section 4 discusses the role of the buoyancy flux and the (de)stabilising mechanisms in the flow. Mixing efficiency is investigated in Section 5. Section 6 studies turbulent diapycnal diffusivity and turbulent Prandtl number. Section 7 gives conclusions and outlook of future work.

2. Experimental data-set of stratified jet

The experimental data-set used in the present study was collected from a stratified jet facility, as sketched in Figure 1, and the cartesian coordinate sets: x_1 corresponds to the horizontal direction; x_3, perpendicular to x_1, corresponds to the opposite direction to gravity.

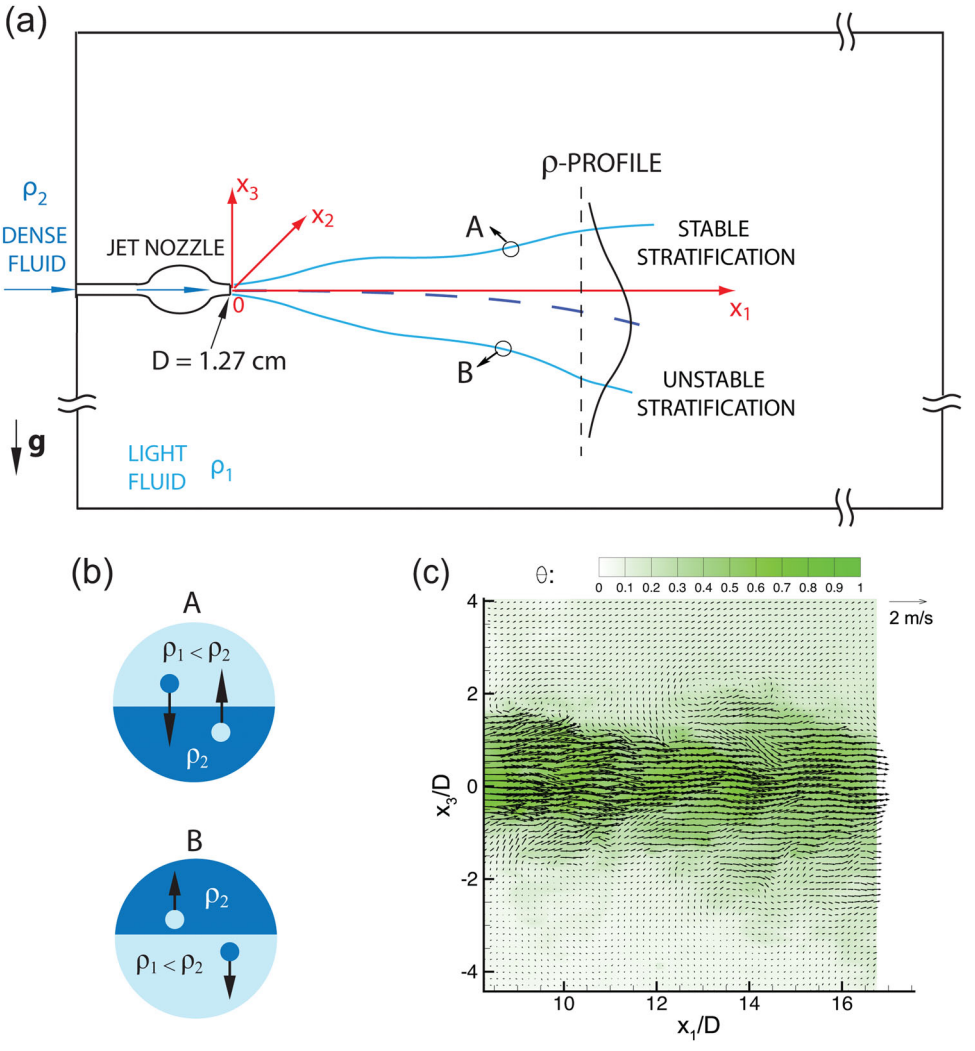

Figure 1. (Colour online) (a) Schematics of the stratified jet facility, where the stable and unstable stratification are highlighted in (b). (c) A representative snapshot of simultaneous velocity and density fields where only 1/4 of the velocity vectors are shown for clarity.

x_1 and x_3 are also referred as the streamwise and vertical direction, respectively. A dense fluid (salt solution, density $\rho_s \simeq 1000.1\ g/L$) was injected through a circular nozzle into a light fluid (ethanol solution, density $\rho_e \simeq 995.0\ g/L$) with a slight density difference ($\delta\rho_o = \rho_s - \rho_e$), initially along x_1. In the upper mixing region of the jet, the dense fluid is below the light fluid (indicated by $\partial\langle\theta\rangle/\partial x_3 < 0$) to form stable stratification, while in the lower mixing region, the dense fluid is above the light fluid (indicated by $\partial\langle\theta\rangle/\partial x_3 > 0$) to form unstable stratification. Thus, this stratified jet experiment introduces unique coexistence of stable stratification (usually weakening the mixing) and unstable stratification (enhancing the mixing) as illustrated in Figure 1.[1]

Simultaneous velocity–density measurements were achieved by combining PIV and PLIF. A fluorescent dye was dissolved into the dense fluid with a specified concentration

Table 1. Experimental conditions of the inlet of the stratified jet.

Parameter	low-*Ri*	high-*Ri*
Nozzle inner diameter D (cm)	1.27	
Inlet density difference $2\delta\rho_o/(\rho_s+\rho_e)$	0.5%	
Reduced gravity $g'=2g(\rho_s-\rho_e)/(\rho_s+\rho_e)$ (m/s^2)	0.049	
Schmidt number Sc	500 ∼ 700	
Inlet velocity $U_o=\langle u_1\rangle$ (m/s)	1.9	0.25
Inlet turbulent intensity u_{rms}/U_o	4.5%	3.5%
Inlet Reynolds number $Re_o=U_oD/\nu$	24,000	3,200
Inlet bulk Richardson number $Ri_o=g'D/U_o^2$	0.0002	0.01
Estimated dissipation rate $\epsilon=u_{rms}^3/D$ (m^2/s^3)	0.11	0.00004
Kolmogorov scale $\eta_k=(\nu^3/\epsilon)^{1/4}$ (mm)	0.05	0.38
Batchelor scale $\eta_b=\eta_k/\sqrt{Sc}$ (mm)	0.002	0.016
PIV neighbouring vector distance δ_v (mm)	$0.86\simeq 17\eta_k$	$0.89\simeq 2.4\eta_k$
PLIF pixel resolution δ_θ (mm)	$0.054\simeq 18\eta_b$	$0.056\simeq 3.5\eta_b$

for PLIF measurements. Seeding particles were uniformly added into both the dense and light fluids for PIV measurements. To collect the data used in the present study, a laser sheet illuminated the central vertical plane (x_1, $x_2=0$, x_3) of the jet. Two CCD cameras equipped with filters were used to record separated PIV and PLIF images, respectively. The optics and cameras can be translated along the x_1 direction for measurements at different downstream frames. The scalar data from PLIF were then spatially sub-sampled to match the resolution of the PIV measurements. The characteristic errors of instantaneous measurements are 0.7% for the velocity and 2% for the scalar. A sample pair of the instantaneous velocity and density fields on a resolved 128 × 128 grid is shown in Figure 1. More details of the experimental setup, the PIV–PLIF technique and the calibration procedure as well as the uncertainty analysis can be found in Ref [43].

Data from two sets of experiments are analysed in the present study, as summarised in Table 1. The first set, termed 'low-*Ri* case', has an inlet velocity $U_o=1.9$ m/s with 0.5% density difference, where the bulk Richardson number is 0.0002. The second set (termed 'high-*Ri* case') has a reduced inlet velocity $U_o=0.25$ m/s with 0.5% density difference to achieve a bulk Richardson number of 0.01. For the low-*Ri* case, data were collected from three consecutive downstream frames spanning from $x_1/D=0$ to 25, where the field of view for each frame is 11 × 11 cm^2. For the high-*Ri* case, measurements were conducted from $x_1/D=0$ to 18.5. At each frame, a large amount of snapshots (600 for low-*Ri* case and 2000 for high-*Ri* case) were recorded in multiple runs to form ensemble sets for converged statistical analysis. The Reynolds decomposition is applied to the velocity–density data to obtain the ensemble averaged terms ($\langle u_i\rangle$ and $\langle\theta\rangle$) and the fluctuation terms (u_i' and θ'), respectively. In the present study, the data in the jet core, identified by $\langle\theta\rangle\le 0.2$, are used in data analysis to prevent the contamination of noise from the nearly quiescent background. One is reminded that both cases (even labeled as 'low-*Ri*' and 'high-*Ri*' cases in the present study) still fall in the category of conventionally defined low Richardson number region, where gradient Richardson number is less than a critical value 1/4, so the turbulence effect is significant (in the present low-*Ri* case) or at least cannot be neglected (in the present high-*Ri* case).

3. Estimation of turbulent energetics

The simultaneous velocity–density data-set in the present study enables direct analysis of the turbulent energetics terms in Equations (1). In particular, $\mathcal{B}$ is computed directly from

its definition (Equation 3). The analysis of $\mathcal{P}$ requires all elements of Reynolds stress tensor $\langle u_i' u_j' \rangle$ and mean strain rate tensor S_{ij}. In this study, the symmetry of mean flow in reference to central $x_1 - x_3$ plane leads to

$$\langle u_2 \rangle_{(x_1,0,x_3)} = 0, \quad \left\langle \frac{\partial u_2}{\partial x_1} \right\rangle_{(x_1,0,x_3)} = \left\langle \frac{\partial u_2}{\partial x_3} \right\rangle_{(x_1,0,x_3)} = 0, \tag{8}$$

and

$$\left\langle \frac{\partial u_1}{\partial x_2} \right\rangle_{(x_1,0,x_3)} = \left\langle \frac{\partial u_2}{\partial x_2} \right\rangle_{(x_1,0,x_3)} = \left\langle \frac{\partial u_3}{\partial x_2} \right\rangle_{(x_1,0,x_3)} = 0, \tag{9}$$

then all resolved terms from planar PIV measurements within (x_1, 0, x_3), i.e. $u_1(x_1, x_3)$, $u_3(x_1, x_3)$ and $u_1'(x_1, x_3)$, $u_3'(x_1, x_3)$ as well as their spatial derivatives, enable direct analysis of $\mathcal{P}$ without assumptions:

$$\mathcal{P} = -\langle u_1'^2 \rangle \frac{\partial \langle u_1 \rangle}{\partial x_1} - \langle u_1' u_3' \rangle \frac{\partial \langle u_1 \rangle}{\partial x_3} - \langle u_1' u_3' \rangle \frac{\partial \langle u_3 \rangle}{\partial x_1} - \langle u_3'^2 \rangle \frac{\partial \langle u_3 \rangle}{\partial x_3}. \tag{10}$$

The accurate analysis of ϵ using PIV data is a challenging task [see, e.g., 44–47]. In this study, ϵ is estimated from all the resolved terms:

$$\begin{aligned} \epsilon \simeq \alpha \cdot \nu \Bigg\langle & 4\left(\frac{\partial u_1'}{\partial x_1}\right)^2 + 4\left(\frac{\partial u_3'}{\partial x_3}\right)^2 + 4\left(\frac{\partial u_1'}{\partial x_1}\right)\left(\frac{\partial u_3'}{\partial x_3}\right) \\ & + 3\left(\frac{\partial u_1'}{\partial x_3}\right)^2 + 3\left(\frac{\partial u_3'}{\partial x_1}\right)^2 + 6\left(\frac{\partial u_1'}{\partial x_3}\right)\left(\frac{\partial u_3'}{\partial x_1}\right) \Bigg\rangle, \end{aligned} \tag{11}$$

where the unresolved terms are approximated by a local isotropy assumption [48] as used in field measurements of oceanic flows.[49] Here, α is a correction coefficient introduced in Ref [47], to account for the effect of limited PIV resolution (i.e., $\alpha \simeq 10$ for the low-Ri case and $\alpha \simeq 1.0$ for the high-Ri case). This correction is necessitated for the data of low-Ri where $\delta_v/\eta_k \gg 1$ (where δ_v is the PIV resolution and η_k is the Kolmogorov length scale, see details in Table 1).

In this study, the velocity gradients are obtained by applying a least-squares filter operation on five neighbouring points on the PIV grids, e.g.,

$$\left.\frac{\partial u_i}{\partial x_j}\right|_{(m,n)} \simeq \frac{-2u_i|_{(m,n-2)} - u_i|_{(m,n-1)} + u_i|_{(m,n+1)} + 2u_i|_{(m,n+2)}}{10\delta_v} \tag{12}$$

to reduce the computation error using PIV data.[50] Similarly, the scalar gradient is evaluated by

$$\left.\frac{\partial \theta}{\partial x_j}\right|_{(m,n)} \simeq \frac{-2\theta|_{(m,n-2)} - \theta|_{(m,n-1)} + \theta|_{(m,n+1)} + 2\theta|_{(m,n+2)}}{10\delta_\theta}, \tag{13}$$

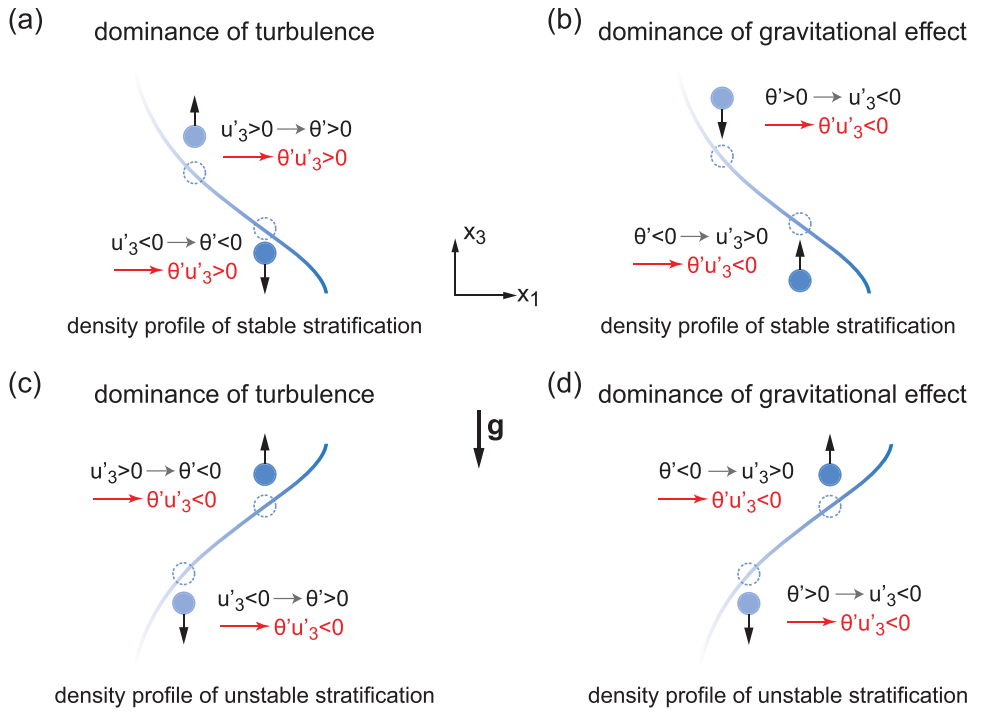

Figure 2. (Colour online) The sketch of the correlation between θ' and $\theta' u_3'$ for illustrating the role of $\mathcal{B}$: (a) and (c) the dominance of turbulence; (b) and (d) the dominance of gravitational effect, in the stable stratification region (a) (b) and the unstable stratification region (c) (d).

where δ_θ is the PLIF pixel resolution. δ_v and δ_θ are summarised in Table 1. In addition, the mean scalar gradient along x_3 direction, $\partial\langle\theta\rangle/\partial x_3$ is used to differentiate the two stratification regions: positive value for unstable stratification and negative value for stable stratification.

4. Effect of buoyancy flux

In Equation (1), the roles of $\mathcal{P}$ and ϵ serving as the TKE generation and the TKE consumption, respectively, remain the same in both stable and unstable stratification regions. The buoyancy flux $\mathcal{B}$ manifests a TKE consumption when $\mathcal{B} > 0$ or a TKE generation when $\mathcal{B} < 0$. The role of $\mathcal{B}$ may also alter in the same stratification conditions. The correlation between θ' and u_3' is presented here to illustrate the mechanisms underlying the effect of $\mathcal{B}$ (i.e., average of $g'\theta' u_3'$). In this analysis, the mean scalar field $\langle\theta\rangle(x_3)$ represents the background stratification once the jet is established. Two effects, namely turbulent effect (i.e., inertia dominant) and gravitational effect (i.e., buoyancy dominant), compete to bring in small perturbations (or fluctuations) to the stratification:

(1) When turbulent effect dominates: In the stable stratification region (see Figure 2(a)), inertia of turbulent motion may agitate a fluid parcel up ($u_3' > 0$) along the gravitational direction away from its neutral position (of $\langle\theta\rangle(x_3)$) to locate in a light ambient, and the fluid parcel has $\theta' > 0$. Similarly, turbulence may agitate a fluid parcel

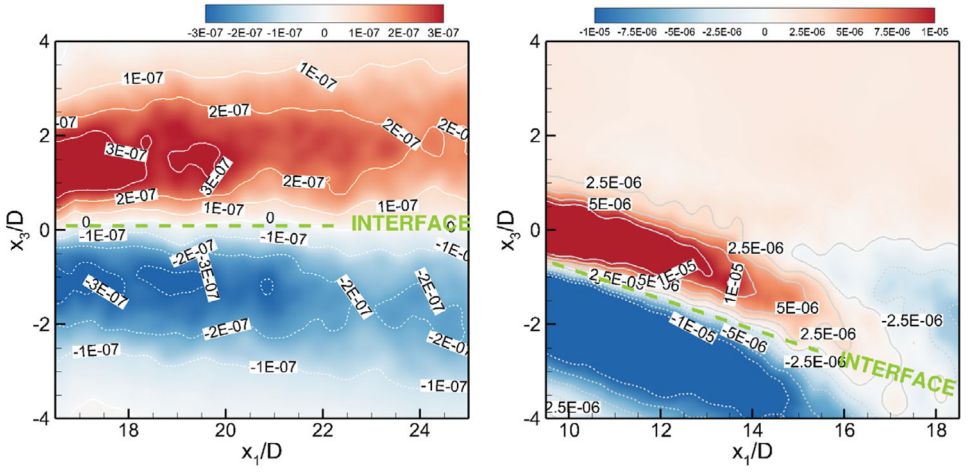

Figure 3. Distributions of $\mathcal{B}$ in low-*Ri* case (left) and high-*Ri* case (right). The region with $\mathcal{B}$ is contour coded and positive marked by solid lines while the negative by dotted lines. The interface between the stable and unstable stratification regions is marked by a thick dashed line. Labelled are local values of $\mathcal{B}$ normalised by $\langle U_0 \rangle^3/D$.

down ($u_3' < 0$) resulting in $\theta' < 0$. This scenario will lead to a positive correlation $\theta' u_3' > 0$. In the unstable stratification region (see Figure 2(c)), turbulence brings a fluid parcel down ($u_3' < 0$) and leads to $\theta' > 0$ (or bring a fluid parcel up $u_3' > 0$ and lead to $\theta' < 0$), resulting in a negative correlation $\theta' u_3' < 0$.

(2) When gravitational effect dominates: In the stable stratification region (see Figure 2(b)), the gravitational effect drives a parcel of heavy fluid ($\theta' > 0$) moving down ($u_3' < 0$), resulting in $\theta' u_3' < 0$. In the unstable stratification region (see Figure 2(d)), the gravitational effect prevents a parcel of heavy fluid ($\theta' > 0$) from restoring to its original position, but drives the fluid parcel to move further along the gravity ($u_3' < 0$), resulting in $\theta' u_3' < 0$.

Consequently, in the stable stratification region, the ensemble buoyancy flux $\mathcal{B}$ indicates the overall competition of a stabilising mechanism and another destabilising mechanism (referring to restoring of the TKE) from the above-mentioned two effects. When turbulence is dominant, $\mathcal{B} > 0$ in the stable stratification region represents a stabilising effect, whereas $\mathcal{B} < 0$ in the unstable stratification region represents a destabilising effect. When gravitational effect is dominant, $\mathcal{B}$ is always negative in both regions, thus always represents a destabilising effect. In flows with coexistence of stable and unstable stratifications, like the present study, $\langle \theta' u_3' \rangle > 0$ indicates the stabilising mechanism dominates, where $\mathcal{B}$ assists ϵ as sink terms in Equation (1). At the same time, $\mathcal{B} < 0$ elucidates that the destabilising mechanism dominates, where $\mathcal{B}$, as a source term, helps the buildup of the TKE. In the unstable stratification region, both the turbulence and the gravitational effect serve as destabilising mechanisms to cause $\langle \theta' u_3' \rangle < 0$.

In Figure 3, $\mathcal{B} < 0$ is observed in the unstable stratification region of both low-*Ri* and high-*Ri* cases, as expected. $\mathcal{B} > 0$ exists in the stable stratification region of low-*Ri* case

where the turbulence dominates. In contrast, $\mathcal{B} > 0$ and $\mathcal{B} < 0$ coexist in the stable stratification region of high-*Ri* case. In this region at further downstream locations, the turbulence decays and the gravitational effect becomes significant, as indicated by the sign change of $\mathcal{B}$.

In the high-*Ri* case, the buoyancy effect is significant. The potential energy in the unstable stratification region is converted to the kinetic energy of the mean flow, then to TKE, and eventually is dissipated by viscous process. The overall loss of the potential energy is indicated by the global jet bending down. Because the stable stratification region is adjacent to the unstable stratification region, the same bending down occurs due to continuity across the stable–unstable interface. As a result, the potential energy in the stable stratification region has to be converted to the kinetic energy as well. One is reminded if only stable stratification exists when buoyancy effect is significant, the jet loses its kinetic energy so the potential energy increases. A similar situation exists at the upstream of the jet where the jet bending by the unstable stratification is not yet developed. This difference in the stable stratification region is indicated by the transition of $\mathcal{B}$ from a positive value (upstream) to a negative value (downstream).

5. Mixing efficiency

Because $\mathcal{B}$ and $\mathcal{P}$ are evaluated accurately, the local values of mixing efficiency $Ri_f = \mathcal{B}/\mathcal{P}$ (Equation 5) can be directly determined. In general, $Ri_f > 0$ exists in the stable stratification region and $Ri_f < 0$ in the unstable stratification region, due to the sign change of $\mathcal{B}$ and $\mathcal{P} \geq 0$ in these two regions. Here, $\mathcal{P} \geq 0$ suggests a forward energy transfer from large scale mean flow to small scale turbulence, and no net backward energy transfer from small scale to large scale is observed here. Meanwhile, the gradient Richardson number is estimated by

$$Ri_g \approx -g' \frac{\partial \langle \theta \rangle / \partial x_3}{(\partial \langle u_1 \rangle / \partial x_3)^2} \tag{14}$$

since $\partial \langle u_1 \rangle / \partial x_3 \gg \partial \langle u_2 \rangle / \partial x_3$ in this stratified jet. A positive Ri_g corresponds to the stable stratification region while a negative value corresponds to the unstable stratification region. The mixing efficiencies in the stable and unstable stratification regions are analysed separately to quantify the influence of the two stratification mechanisms. The value of Ri_f along the x_3 direction conditionally averaged in the stable or unstable stratification region, $\langle Ri_f \rangle_{x_3}$, is plotted in Figure 4, where $\langle Ri_f \rangle_{x_3}$ in the stable stratification region and $-\langle Ri_f \rangle_{x_3}$ in the unstable stratification region are plotted together for direct comparison of their magnitudes. In the low-*Ri* case, the magnitudes of $\langle Ri_f \rangle_{x_3}$ increase approximately exponentially, and the data points of the stable and unstable stratification regions nearly overlap. $\langle Ri_f \rangle_{x_3}$ for $x_1/D > 18$ are slightly off the exponential trend and approach a constant value. In the high-*Ri* case, the two curves are separated: $\langle Ri_f \rangle_{x_3}$ in the unstable stratification region roughly remains the exponential increasing, when $\langle Ri_f \rangle_{x_3}$ from the stable stratification region decreases slightly after remaining as constant for $x_1/D < 9$.

To understand the scale-dependence of Ri_f, we examine the spectra of Ri_f within the stable and unstable stratification regions, respectively. The spectra are computed using the data from the chosen zones marked in Figure 5. The averaged Ri_f from five neighbouring PIV

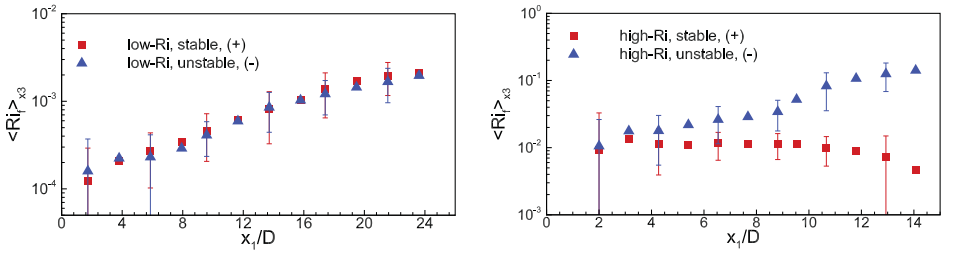

Figure 4. (Colour online) The development of x_3-averaged Ri_f in stable and unstable stratification regions: (left) low-*Ri* case and (right) high-*Ri* case. $-\langle Ri_f \rangle_{x_3}$ in unstable stratification region is plotted with $+\langle Ri_f \rangle_{x_3}$ in stable stratification region for direct comparison of magnitudes. The error bars show the standard deviation.

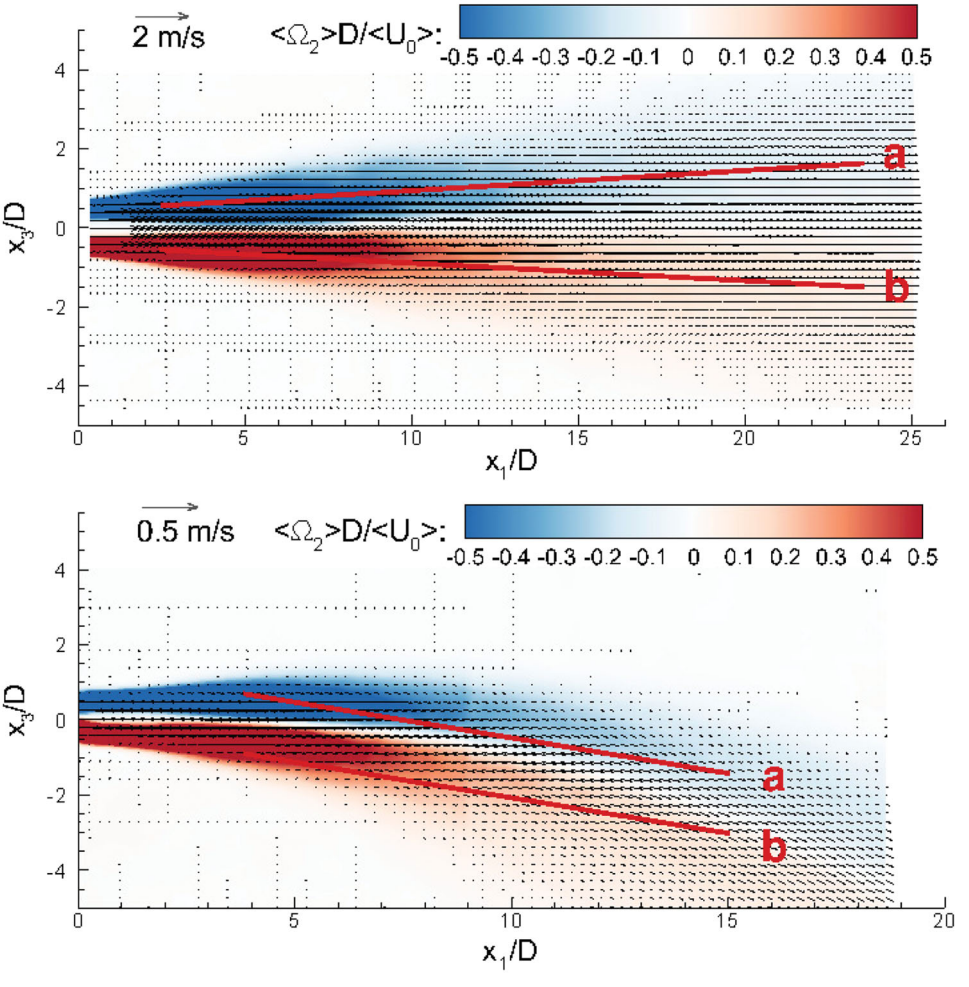

Figure 5. Contours of the mean vorticity component $\langle \Omega_2 \rangle$ for low-*Ri* case (top) and high-*Ri* case (bottom). The vectors represent the in-plane velocity components: $\langle u_1 \rangle$ and $\langle u_3 \rangle$, and 1/9 of the vectors are plotted for clarity. The marked zones (a and b) indicate the ranges of data used for one-dimensional spectra of Ri_f.

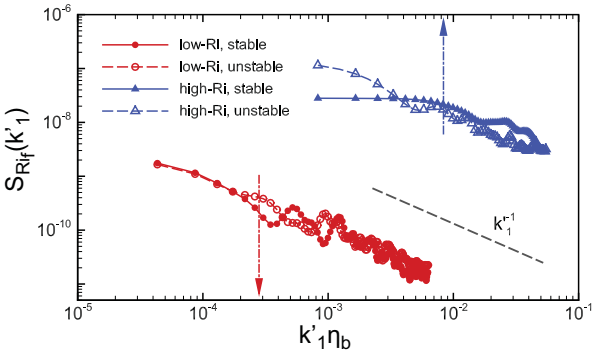

Figure 6. (Colour online) The one-dimensional spectra of Ri_f in stable and unstable stratification regions for low-*Ri* and high-*Ri* cases. The grey dash line indicates a decay law of $k_1'^{-1}$. η_b is the Batchelor scale indicated in table 1. The arrow marks the Ozmidov length scale.

grid points in x_3 direction is retrieved along the preferred direction and linear interpolations are perform if necessary. The preferred directions are chosen to include the maximum number of available data points in the core part of the jet (stable or unstable). The 1D spectrum $\mathcal{S}_{Ri_f}(k_1')$ is obtained by applying Fourier transforms to the retrieved data, where k_1' indicates the wavenumber corresponding to the preferred direction.

In Figure 6, $\mathcal{S}_{Ri_f}(k_1')$ from both stratification regions of the low-*Ri* case decays monotonously as $k_1'^{-1}$. One is noted that the horizontal axis is normalised by the Batchelor scale η_b, which represents the smallest length scale before the scalar fluctuations are dominated by molecular diffusion.[51] In the high-*Ri* case where the buoyancy effect is significant, distinct difference of the spectra in two stratification regions is observed: $\mathcal{S}_{Ri_f}(k_1')$ in the stable stratification region is nearly constant until $k_1'\eta_b \simeq 8 \times 10^{-3}$, which corresponds to the averaged Ozmidov length scale $L_{\mathrm{OZ}} = \sqrt{\epsilon/N^3}$ (smallest length scale of overturning). Beyond that range, $\mathcal{S}_{Ri_f}(k_1')$ decreases following the scaling $1/k_1'$ as $k_1'\eta_b$ increases. $\mathcal{S}_{Ri_f}(k_1')$ in the unstable stratification region of high-*Ri* case, however, monotonously decays as $k_1'^{-1}$ for all length scales. The observed plateau of $\mathcal{S}_{Ri_f}(k_1')$ at the length scales larger than L_{OZ}, in the stable stratification region of high-*Ri* case, illustrates that the mixing efficiency is mainly contributed by all eddy motions larger than the Ozmidov length scale and smaller than the integral scale. On the other side, in the unstable stratification region of the high-*Ri* case, the largest contribution to Ri_f is from the largest eddy motions corresponding to the integral scale. Such a difference suggests that in the stable stratification region of high-*Ri* case, the stratification mainly influences the mixing structure with length scales larger than L_{OZ}, i.e., the eddy sizes of effective mixing in the stable stratification are larger than the local L_{OZ}. In the low-*Ri* case, the momentum effect along the streamwise direction dominates the mixing in the shear layer and suppresses the buoyancy effect, which leads to the approximate equal magnitudes of Ri_f in the stable and unstable stratification regions.

As summarised in Section 1, it is challenging to directly quantify Ri_f in numerical simulations, thus it necessitates an appropriate model, usually by relating Ri_f to Ri_g. By assuming local thermodynamic equilibrium in a homogeneous two-dimensional (2D) flow,[8] the

first modelling was proposed as:

$$Ri_f = 0.5 - 0.5\sqrt{1 - 12\eta Ri_g}, \tag{15}$$

with $\eta \simeq 1$ assumed. The validity of this model depends on the neglected mean flow advection. Later, by applying the energy redistribution hypothesis of Rotta and local isotropy hypothesis of Kolmogorov to close the transport equation of TKE (and scalar variance),[9] Mellor and Yamada proposed the elaborated model:

$$Ri_f = 0.725\left(Ri_g + 0.186 - \sqrt{Ri_g^2 - 0.316Ri_g + 0.0346}\right), \tag{16}$$

which has been largely applied to simulations of geophysical flows. One-point closure models of momentum and vertical thermal diffusivities were proposed to improve the estimate of the nonlocal, third-order moments, yielding a critical gradient Richardson number, $Ri_{g,c} \sim 1$ (above which turbulence ceases to exist. $Ri_{g,c} = 0.25$ is obtained from the linear instability analysis,[52,53] while $Ri_{g,c} > 1$ is obtained from a nonlinear analysis [11,54]). Later, a different model, $\gamma_f = \mathcal{B}/\epsilon = Ri_f/(1 - Ri_f) = 0.01 + Ri_g - 0.053Ri_g^2$, was proposed in [16] to model the mixing efficiency. Converted to the definition of mixing efficiency adopted in the present study, this parameterisation is equivalent to:

$$Ri_f = \frac{0.01 + Ri_g - 0.053Ri_g^2}{1.01 + Ri_g - 0.053Ri_g^2}. \tag{17}$$

By discarding two outlier points, a recent fit to the same data-set [17] yields

$$Ri_f = \frac{0.005 + 1.7Ri_g - 1.1Ri_g^2}{1.005 + 1.7Ri_g - 1.1Ri_g^2}. \tag{18}$$

The present experimental data-set is applied to examine the statistical relationship between Ri_f and Ri_g and to compare with predictions of the aforementioned models. Figure 7(a) shows the two-dimensional histogram plot of Ri_f and Ri_g for the low-Ri case. In both stable and unstable stratification regions, $Ri_f \simeq Ri_g$ can be observed as marked by the dash line when $-0.0025 < Ri_g < +0.0025$ (indicating a 'near neutral' regime [15]). This finding validates the similar discovery ($Ri_f \simeq Ri_g$) from the experimental study of gravity current.[55] However, the results of high-Ri case indicate different trends as shown in Figure 7(b). In the unstable stratification region of the high-Ri case, $Ri_f \simeq Ri_g$ for $-0.02 < Ri_g < 0$, and then for $Ri_g < -0.02$, Ri_f shows a steeper linear relationship with Ri_g. In the stable stratification region of high-Ri case, Ri_f increases nearly linearly ($Ri_f \simeq Ri_g$) when $0 \leq Ri_g \leq 0.02$, but decreases when $0.02 < Ri_g < 0.05$ ('near neutral' regime).

The observed negative values of Ri_f in the range of $0.05 < Ri_g < 0.08$ corresponds to the emergence of negative $\mathcal{B}$ in the stable stratification region. The transition to the countergradient buoyancy flux implies that the dominant stabilising mechanism introduced by turbulence starts to recede ($x_1/D < 16.5$), to be balanced ($x_1/D \simeq 16.5$) and to be overcome ($x_1/D > 16.5$) by the destabilising mechanism from gravitational effect. This countergradient buoyancy flux (also reported previously, e.g., [56]) makes the $Ri_f - Ri_g$ relationship

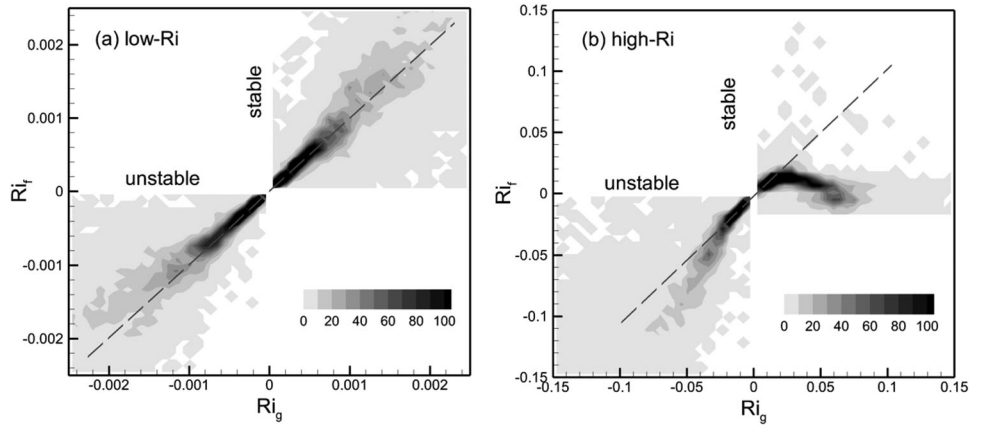

Figure 7. Two-dimensional histogram of Ri_f against Ri_g for (a) low-*Ri* and (b) high-*Ri*. The dash line indicates the trend of $Ri_f = Ri_g$. Contour legend gives the relative level of the histogram (maximum value 100).

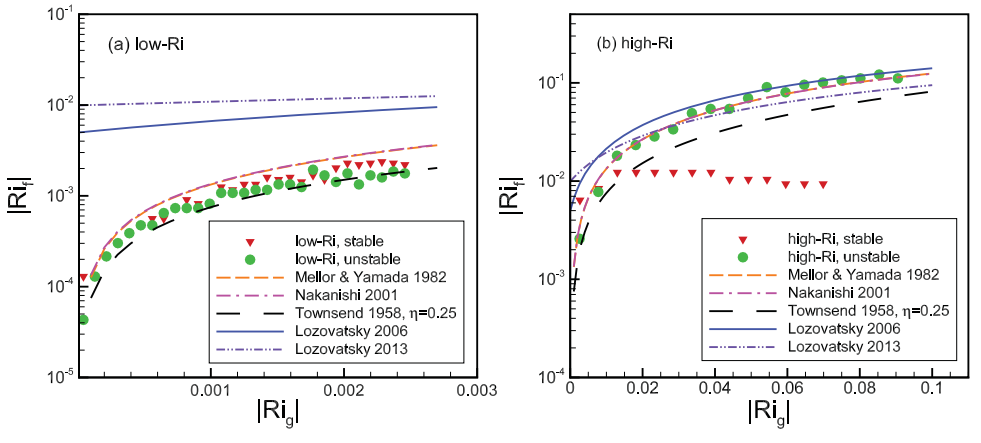

Figure 8. (Colour online) The relationship between Ri_f and Ri_g retrieved from the two-dimensional histogram (figure 7), and compared with the previous reported results. $\eta = 0.25$ is applied in [8] model as suggested in [15].

more complicated than what is described by the existing models [e.g., 8,9], where no competition between stabilising and destabilising mechanisms exists. The present $Ri_f - Ri_g$ data are compared with previous laboratory and field measurements in Figure 8. The data points in both the stable and unstable stratification regions of the low-*Ri* case (near the neutral regime) locate between the predictions of Townsend-model (Equation (15) with $\eta = 0.25$) and those of the Mellor–Yamada model (Equation 16). The other models (Equations 17 and 18) yield predictions of Ri_f whose magnitudes are two decades larger than the experimental data when $|Ri_g| < 0.0002$. For the unstable stratification region of high-*Ri* case shown in Figure 8(b), the Mellor–Yamada model (Equation 16) together with the Lozovatsky model (Equation 17) represent better fits to the experimental data for $Ri_g < 0.1$. However, none of the models predicts Ri_f effectively in the stable stratification region, which indeed presents a new challenge for modelling the mixing efficiency using Ri_g.

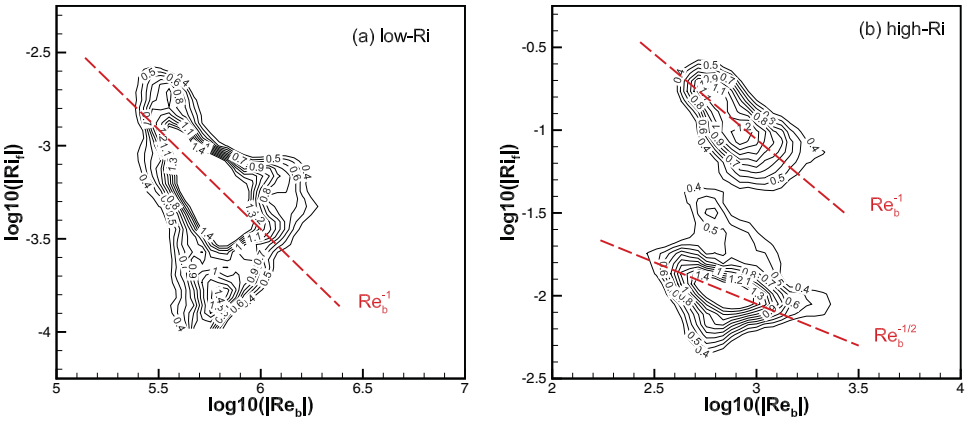

Figure 9. Two-dimensional PDF of Ri_f–Re_b for (a) low-*Ri* where data from (un)stable stratification collapse and (b) high-*Ri* where data from (un)stable stratification separate distinctly with the top pile from the unstable stratification and the bottom pile from the stable stratification.

In most oceanic applications where the mean gradients along x_3 −direction are usually dominant, Ri_f and Ri_g can be estimated through simplified expressions:

$$Ri_f = \frac{\mathcal{B}}{\mathcal{P}} = \frac{g'\langle\theta' u_3'\rangle}{-\langle u_i' u_j'\rangle S_{ij}} \simeq -g' \frac{\langle\theta' u_3'\rangle}{\langle u_1' u_3'\rangle \partial\langle u_1\rangle/\partial x_3}, \tag{19}$$

and

$$Ri_g = \frac{N^2}{S^2} = \frac{(-g/\rho_0)\partial\langle\rho\rangle/\partial x_3}{(\partial\langle u_i\rangle/\partial x_j + \partial\langle u_j\rangle/\partial x_i)^2} \simeq -g' \frac{\partial\langle\theta\rangle/\partial x_3}{(\partial\langle u_1\rangle/\partial x_3)^2}. \tag{20}$$

The $Ri_f - Ri_g$ models thus essentially relate $\langle u_1' u_3'\rangle$ (and $\langle\theta' u_3'\rangle$) to the mean gradients $\partial\langle u_1\rangle/\partial x_3$ (and $\partial\langle\theta\rangle/\partial x_3$). The performance of these models relies considerably on the eddy viscosity/diffusivity assumptions. The traditional eddy viscosity/diffusivity models and their modifications (e.g., κ-profile parameterisation models [57,58]) are widely used in ocean and climate simulations. They assume a positive alignment between $\langle u_i' u_j'\rangle$ and $\partial\langle u_i\rangle/\partial x_j$ (or between $-\langle\theta' u_i'\rangle$ and $\partial\langle\theta\rangle/\partial x_i$). This fundamental assumption often constrains their prediction of, e.g., the counter-gradient buoyancy flux in the stable stratification region in this study.

Furthermore, recent studies argue whether Ri_g alone is adequate to model Ri_f, and it is suggested to adopt Re_b instead as the model variable. The recent study reported field measurements of a mixing parameter γ_f ($= \mathcal{B}/\epsilon = Ri_f/(1 - Ri_f)$, another definition of mixing efficiency) in the stable stratification region against Ri_g and Re_b.[17] The results yield $\gamma_f \sim Re_b^{-1/2}$ (see Figure 7 of [17]). Motivated by this finding, we use the present experimental data to explore the statistical relationship between Ri_f and Re_b. As shown in Figure 9, the data in stable and unstable stratification regions of the low-*Ri* case distribute concentratively, and $|Ri_f|$ decreases loosely as power law of Re_b^{-1}. However, in the high-*Ri* case, the data of the unstable stratification region decay following a similar Re_b^{-1} trend, while the data of stable stratification region decay approximately following a $Re_b^{-1/2}$ trend. Nevertheless,

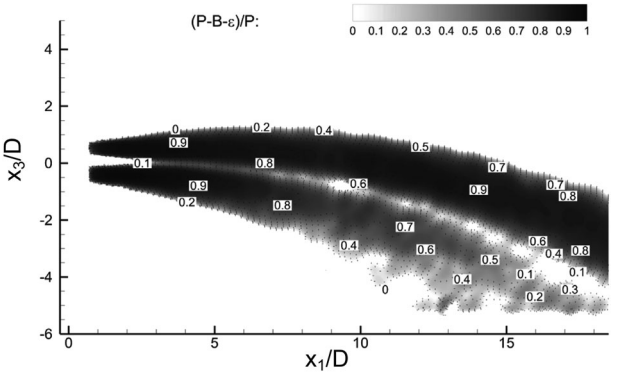

Figure 10. Distribution of $(\mathcal{P}-\mathcal{B}-\epsilon)/\mathcal{P}$ of the high-*Ri* case.

the current data span over a limited range of Re_b due to limited scales in the laboratory experiments, and the 2D PDF shows a rather scattered distribution between Ri_f and Re_b and does not demonstrate a very strong power law correlation, whereas it is noticeable that there are two different $Ri_f - Re_b$ relationships observed in the stable and unstable stratification regions of the high-*Ri* case. With assuming $\mathcal{P}-\epsilon-\mathcal{B}\simeq 0$,[17] Equation (5) can be written as

$$Ri_f = \frac{\mathcal{B}}{\mathcal{P}} \simeq \frac{\mathcal{B}}{\mathcal{B}+\epsilon} = \frac{1}{1+\nu Re_b N^2/\mathcal{B}} = \frac{1}{1+Re_b \nu \kappa_\theta^{-1}}, \tag{21}$$

by applying the eddy-diffusivity assumption $\langle\theta' u_3'\rangle = -\kappa_\theta \partial\langle\theta\rangle/\partial x_3$ (κ_θ is turbulent diffusivity) to represent $\mathcal{B} = g'\langle\theta' u_3'\rangle = \kappa_\theta N^2$. When $Re_b \gg \kappa_\theta/\nu$, one has $Ri_f \sim Re_b^{-1}$, which captures the trend of the elongated contour in the low-*Ri* case and the unstable stratification region of the high-*Ri* case but fails in the stable stratification region of high-*Ri* case. The difference of $Ri_f \sim Re_b^{-1/2}$ from other regimes is possibly contributed by: (a) the failure of assumption $\mathcal{P}-\epsilon-\mathcal{B}\simeq 0$, which was originally proposed under the premise of homogenous stationary turbulence and the transport terms of TKE are negligible. Figure 10 shows $\mathcal{P}-\mathcal{B}-\epsilon$ may be significantly larger than zero, e.g., $(\mathcal{P}-\mathcal{B}-\epsilon)/\mathcal{P}\sim 0.8$ at $x_1/D = 15$ of the stable stratification region and $(\mathcal{P}-\mathcal{B}-\epsilon)/\mathcal{P}\sim 0.4$ in the unstable stratification region. (b) In the stable stratification region, there is a complicated competition between the stabilising mechanism and the destabilising mechanism, as discussed in Section 4, which is distinct from the case where only stable stratification is present. A proposed two-parameter model,[17] $Ri_f \sim f(Re_b, Ri_g)$, shows an improvement over the former single parameter models (e.g., $Ri_f \sim f(Re_b)$ or $Ri_f \sim f(Ri_g)$), but our tests using the present experimental data-set do not lead to further evidence to support this claim. The possible reasons may include: (a) the present laboratory data-set only covers a limited range of the length and time scales, which may be inadequate to reveal the underlying relationship (in [17] $Ri_f - Re_b$ relationship is found over a wider range of length scales: $Re_b \in [10^{3.5} \sim 10^{7.5}]$ and $Ri_g \in [10^{-3} \sim 10^{0.5}]$); (b) whether Ri_g and Re_b are independent of each other remains an open question: for example, laboratory experiments of gravity currents showed $\mathcal{P}/\mathcal{B} = 1/Ri_f = L_m^2 Ri_g^{-1}/L_\theta^2$,[55] where L_m and L_θ are mixing lengths. If this relationship

and the one in Equation (21) are treated equally valid, one may obtain a dependence relationship between Ri_g and Re_b: $L_m^2 L_\theta^{-2} Ri_g^{-1} \simeq 1 + \nu\kappa_\theta Re_b$. In addition, adopting Re_b as one of the model parameters (or the only one) will introduce extra difficulties since quantifying Re_b needs explicit knowledge of ϵ which is usually difficult to estimate accurately in simulations. More research efforts from field measurements and laboratory data may elucidate these concerns.

6. Turbulent diapycnal diffusivity and turbulent Prandtl number

Turbulent diapycnal diffusivity, $\kappa_\theta = \mathcal{B}/N^2$,[59] quantifies the scalar diffusion in the vertical direction due to turbulent fluctuations. It can also be interpreted as the model coefficient in the eddy-diffusivity models. Several parameterisations of κ_θ have been developed from theoretical, experimental and numerical studies. By assuming a stationary balance between the source and sink of TKE, κ_θ can be expressed in terms of the flux Richardson number [59]:

$$\kappa_\theta = \frac{\epsilon}{N^2} \frac{Ri_f}{1 - Ri_f}. \tag{22}$$

It is suggested that $Ri_f \leq 0.17$ and thus $\gamma_f = Ri_f/(1 - Ri_f) \leq 0.2$,[59] and $Ri_f = 0.17$ and $\gamma_f = 0.2$ are usually adopted as a common practice.[60] Equation (22) implies κ_θ is explicitly independent of the molecular diffusivity κ and the kinematic viscosity ν. κ_θ is often related to ϵN^{-2} in numerical models [11] and field measurements.[17] In a laboratory study of linearly stably stratified flows with different Prandtl number,[21] κ_θ was found to be characterised by Re_b in two regimes, i.e.,

$$\kappa_\theta = \begin{cases} 0.9\nu^{2/3}\kappa^{1/3}Re_b & \text{for} \quad Re_b < 300 \\ 2\nu^{2/3}\kappa^{1/3}Re_b^{1/3} & \text{for} \quad Re_b > 300 \end{cases}, \tag{23}$$

where in both regimes κ_θ depends on ν and κ. Later DNS of a homogeneous sheared stratified flow (Prandtl number ~0.7) suggested a three-regime parameterisation [20], i.e.,

$$\kappa_\theta = \begin{cases} \sim \kappa & \text{for} \quad Re_b \sim \mathcal{O}(1) \\ 0.2\nu Re_b & \text{for} \quad 10 < Re_b < 100 \\ 2\nu Re_b^{1/2} & \text{for} \quad Re_b > 100 \end{cases}. \tag{24}$$

In the diffusive regime ($Re_b \sim \mathcal{O}(1)$) κ_θ is close to molecular diffusivity, and in the other two regimes, κ_θ explicitly depends on ν.

In the present study, to match the refractive indices, only one combination of dense and light fluids can be chosen, so the fluidic parameters (κ and ν) remain the same in different cases. The experimentally determined κ_θ–Re_b relationship is compared to the models of [21] and [20] in Figure 11. The models are developed for homogeneous stably stratified turbulence, so the results from the stable stratification region are directly compared with model predictions. The results from the unstable stratification region are examined to determine if these models can be extended to the unstable stratification region as well. For the low-Ri case, κ_θ in both stable and unstable stratification regions shows an increasing trend as Re_b increases, where the data in the stable stratification region nearly overlap

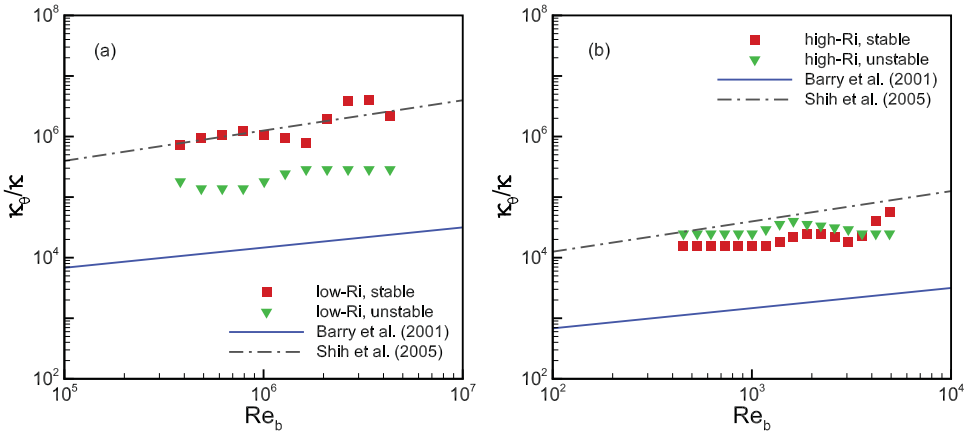

Figure 11. (Colour online) Turbulent diffusivity κ_θ versus buoyancy Reynolds number Re_b: (a) low-*Ri* case and (b) high-*Ri* case. κ_θ is normalised by the molecular diffusivity of salt in water κ.

with model prediction of [20] while the data points in the unstable stratification region lie between the predictions using models of [21] and [20]. For the high-*Ri* case, κ_θ in both regions are slightly below the predictions of [20] model but show a weak dependence on Re_b. The slightly increasing trend of κ_θ shows the dependence of κ_θ on Re_b in the energetic regime with Re_b up to 10^7, but the scattering of κ_θ (in log-scale) indicates that this dependence is not well converged.

Furthermore, rather than modelling the overall mixing, the irreversible mixing diffusivity,

$$\kappa_\rho = \frac{\epsilon_\theta}{(\partial\langle\theta\rangle/\partial x_3)^2}, \tag{25}$$

was suggested to be modelled individually.[61] κ_ρ can be modelled by

$$\kappa_\rho = \gamma \frac{L_E^2}{T_L}, \tag{26}$$

which is explicitly independent of κ and ν, and γ is a non-dimensional mixing coefficient. By introducing Péclet number Pe_t, the normalised parameterisation is

$$\kappa_\rho/\kappa = \gamma Pe_t. \tag{27}$$

This model was examined using DNS data of homogeneous stably stratified flows [61] and later by other experimental and numerical results.[62]

As shown in Figure 12, our experimental data show a strong linear relationship between κ_ρ/κ and Pe_t between $\gamma = 0.2$ and $\gamma = 0.7$ (reported in [61]). This model (Equation 27) generally is applicable to both the stable and unstable stratification regions, and further investigations of stratified flows with different Sc may further reveal the generality of this parameterisation.

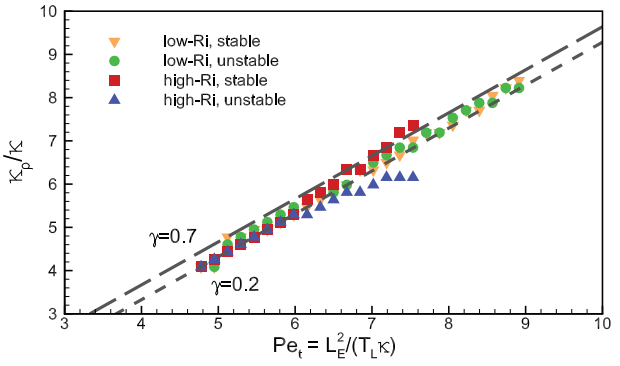

Figure 12. (Colour online) The normalised irreversible turbulent diffusivity (κ_ρ/κ) versus the turbulent Péclet number Pe_t. The long-dash line indicates $\gamma = 0.7$ in Equation (26), and the short dash line indicates $\gamma = 0.2$.

To relate the momentum flux and scalar flux, the turbulent Prandtl number $Pr_t = \kappa_m/\kappa_\theta$ is introduced in studies of stratified turbulence,[7,34,63] where κ_m is the vertical diffusion of momentum (or eddy viscosity). Pr_t is often parameterised with Ri_g, and our experimental data are compared with predictions of four different models of Pr_t as reviewed in [18]. To take account of the effect of stratification on turbulent eddy viscosity and diffusivity, the gradient Richardson number was used in the modelling of κ_m and κ_θ in order to lead to the modelling of Pr_t,[26]

$$Pr_t = Pr_{t0}\frac{(1+\beta_m Ri_g)^{\alpha_m}}{(1+\beta_\theta Ri_g)^{\alpha_\theta}}, \tag{28}$$

where $\beta_m = 10$, $\alpha_m = -1/2$ and $\beta_\theta = 10/3$ as well as $\alpha_\theta = -3/2$ are modelling coefficients retrieved from experiments. Pr_{t0} is the Prandtl number for the neutrally stratified flows (or passive scalar cases). As suggested in [18], combining the results of the Pacific Ocean from [27] for $Ri_g \le 0.25$ and the results of laboratory experiments from [64] for $Ri_g > 0.25$ gives the Pr_t,

$$Pr_t = \begin{cases} (56/3)Ri_g^{7/5} & \text{for} \quad Ri_g \le 0.25 \\ \dfrac{5.0(1.0+5.0Ri_g)^{-3/2}+0.2}{5.0(1.0+5.0Ri_g)^{-2.5}+0.01} & \text{for} \quad Ri_g > 0.25 \end{cases}. \tag{29}$$

One should be noted that different to other models, Pr_t (Equation 29) increases asymptotically to a finite value ($Pr_t \to 20$) when $Ri_g \to \infty$. In addition, this model predicts $Pr_{t0} = 0$ when $Ri_g = 0$ in the neutrally stratified flows, where $\kappa_m = 0.00056Ri_g^{-8.2} = 0$ and $\kappa_\theta = 0.00003Ri_g^{-9.6} = 0$ give an unrealistic result. Based on the Louis model where the mixing length is associated with the Richardson number, another parameterisation of Pr_t was proposed,[28]

$$Pr_t = Pr_{t0}\frac{1+15Ri_g(1+5Ri_g)^{1/2}}{1+10Ri_g(1+5Ri_g)^{-1/2}}, \tag{30}$$

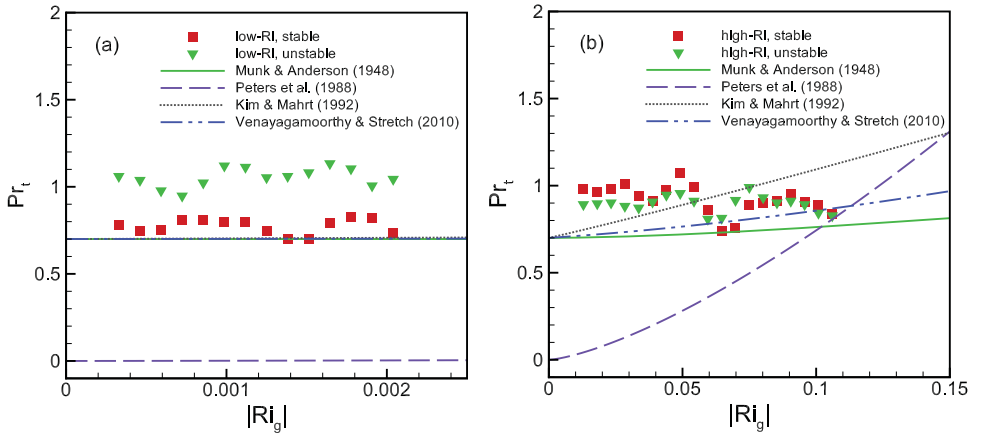

Figure 13. (Colour online) Turbulent Prandtl number Pr_t versus gradient Richardson number Ri_g: (a) the low-*Ri* case and (b) the high-*Ri* case.

where the coefficients were validated experimentally. The most recent parameterisation of Pr_t was proposed in [25], in analogy to their parameterisation of κ_ρ,[61] where κ_m is derived to be associated with κ_ρ in the simplified transport equation of TKE of the homogeneous stably stratified flow. Therefore, one should have

$$Pr_t = Pr_{t0} \cdot \exp\left(\frac{-Ri_g}{Pr_{t0}\Gamma_\infty}\right) + \frac{Ri_g}{Ri_{f\infty}} \tag{31}$$

where $Ri_{f\infty} \simeq 1/4$ and $\Gamma_\infty = Ri_{f\infty}/(1 - Ri_{f\infty}) \simeq 1/3$. One is noted that Equation (31) represents the turbulent Prandtl number of the irreversible mixing process Pr_t^* in an analytical derivation, and the simplified $\mathcal{P} = -\langle u_1' u_3' \rangle \partial \langle u_1 \rangle / \partial x_3$ makes the derived $\kappa_m = \epsilon/(\partial \langle u_1 \rangle / \partial x_3) + Ri_g \kappa_\rho$ invalid in the stratified jet. $Pr_t \simeq Pr_t^*$ is assumed in this study based on the fact that the irreversible mixing is significantly dominant in stratified jet. The $Pr_t - Ri_g$ relationships are examined in Figure 13. For the low-*Ri* case, the experimental data from the unstable stratification region are above the predictions of Equations (28)–(31), while the data from the stable stratification regions are slightly above the model predictions. In the stable stratification region, the buoyancy flux assists the viscous dissipation to dissipate the TKE produced by the shear. In the unstable stratification region, the buoyancy flux helps the mean shear to produce TKE to compete with the viscous dissipation. This possibly explains the difference of Pr_t between the stable and unstable stratification regions in the low-*Ri* case. For the high-*Ri* case, the experimental data from the stable and unstable stratification regions are larger than the predictions of Equations (28) and (31). The experimental data show weak dependence of Pr_t on Ri_g, which cannot be represented by the existing models, especially Equation (29). Pr_t in the stable stratification region is close to that from the unstable stratification region. Pr_{t0} is important for smoothly transit to neutrally stratified (or unstratified) flows. $Pr_{t0} \sim 0.5 - 1.0$ was suggested from numerical and experimental studies [29,65] and $Pr_{t0} \simeq 0.7$ was derived in the theoretical arguments.[61] From the data of neutrally stable stratification (the low-*Ri*) case, $Pr_{t0} \simeq 0.75$ can be retrieved, which falls in $0.7 < Pr_{t0} < 0.9$ [65] and is close to theoretical derived $Pr_{t0} =$

0.7.[25] The existing models for Pr_t and their underlying arguments assume stably stratified turbulence, thus the models are difficult to be applied to, e.g., unstably stratified flows. With an improved parameterisation of Pr_t, which is applicable to more general stratification settings, collapsed data points from the stable and unstable stratification (analogous to κ_ρ in Figure 12) should be expected.

7. Discussion and summary

In this paper, we present an independent study of the mixing dynamics in a stratified jet with coexistence of stable and unstable stratification. The velocity–density data were simultaneously obtained by a combined PIV–PLIF technique, leading to accurate measurements of buoyancy flux $\mathcal{B} = g'\langle\theta' u_3'\rangle$ and production of TKE due to the gradients of mean velocity $\mathcal{P} \equiv -\langle u_i' u_j'\rangle S_{ij}$ (Equation 10). The mixing efficiency, therefore, can be quantified directly through $Ri_f = \mathcal{B}/\mathcal{P}$. In addition, the turbulent diapycnal diffusivity κ_θ (or κ_ρ) and turbulent Prandtl number Pr_t are studied, as well as other discoveries from the meticulous experiments of this unique stratified flow, including:

(1) The correlation between scalar fluctuations and the buoyancy flux demonstrate that the stabilising mechanism (in reference to kinetic energy) produced by turbulence competes with the destabilising mechanism (in reference to kinetic energy) produced by gravitational effect in the stable stratification, while only destabilising mechanism exists in the unstable stratification. Consequently, $\mathcal{B}$ is an ideal indicator of the overall mechanism. The destabilising mechanism is found to be dominant in the stable stratification of high-*Ri* case where the potential energy is converted back to (turbulent) kinetic energy.
(2) The 1D spectra of Ri_f, $S_{Ri_f}(k_1')$, obtained from the stable and unstable stratification regions separately, are shown in Figure 6. In the low-*Ri* case, $S_{Ri_f}(k_1')$ is nearly identical in two stratification regions, and it monotonously decreases as wavenumber increases. The monotonous decreasing trend of $S_{Ri_f}(k_1')$ can also be found in the unstable stratification region of high-*Ri* case, but Ri_f from the stable stratification region is contributed almost evenly at the length scales larger than the Ozmidov length scale. This finding suggests that the eddy sizes larger than the Ozmidov scale are needed to mix the fluids effectively.
(3) Ri_f presents a linear relationship with Ri_g (Figure 7), i.e., $Ri_f \simeq Ri_g$, in the 'neutral' regime (in the low-*Ri* case) but the deviation from this linear description exists in 'near neutral' regime, especially for the stable stratification region of the high-*Ri* case. The Mellor–Yamada model (Equation 16) presents a rational prediction of the $Ri_f - Ri_g$ relationship for the low-*Ri* case and the unstable stratification region of the high-*Ri* case. None of the studied models, however, give decent predictions in the stable stratification region of the high-*Ri* case.
(4) The argument that whether Ri_g is adequate of modelling Ri_f motivates our study of the dependence of Ri_f on Re_b, as suggested in [17]. We discover weak dependence of Ri_f on Re_b following a power law of Re_b^{-1} for both stratification regions of the low-*Ri* case, as well as the unstable stratification region of the high-*Ri* case, but another $Re_b^{-1/2}$ power law for the stable stratification region of the high-*Ri* case is identified. The ambiguous dependence of Ri_f on Re_b does not support $Ri_f \sim f(Ri_g, Re_b)$, which

is potentially due to a limited range of scales in laboratory experiments, as well as the inherent dependence Ri_g on Re_b.

(5) The experimentally determined turbulent diffusivity κ_θ (and κ_ρ, as defined in Equation 25) as well as turbulent Prandtl number Pr_t are examined to appraise the theoretical and empirical models. The increase of κ_θ (quantifying the overall mixing process) against Re_b can be approximately represented by the model of [20] but with discrepancies. On the other side, the turbulent diffusivity of the irreversible mixing process (κ_ρ) demonstrates a converged distribution with Pe_t, and the overlap of data from the stable and unstable stratification regions of two cases illustrates the model of [61] with more general applicability. As a connection between the momentum flux and scalar flux, it is more challenging to parameterise Pr_t. The [25] model presents a relatively better prediction of Pr_t, but the transient-volatile nature of the stable stratification region offers nontrivial challenges to all models of Pr_t. This is because the models are developed by assuming, e.g., the energetic balance $\mathcal{P} = \mathcal{B} + \epsilon$, which fails in the stratified jet because of nontrivial transport term (as indicated in Figure 10). We confirm the neutral turbulent Prandtl number Pr_{t0} ranging between 0.7 and 0.9, and suggest $Pr_{t0} \simeq 0.75$, which is close to $Pr_{t0} \simeq 0.7$ in the homogeneous stably stratified turbulence.

The presented study investigates the unique coexistence of stable and unstable stratification with implications in characterising and modelling mixing dynamics. There are still remaining open questions to be tackled in future studies from both experimental and numerical investigations. In particular, attention should be given to the influence of local concurrence of stable and unstable stratification on the large scale turbulence and the corresponding energetics mechanism. The present work also introduces the need of developing advanced models that are able to describe the local mixing dynamics in stable and unstable stratification region differently.

Note

1. The computational cost of implementing DNS of the same stratified jet is estimated by the procedure in Section 9.1.2 of Ref. [42], where the spatial resolution of DNS is set to the Batchelor length scale $\eta_b = \eta_k/\sqrt{Sc}$ ($Sc \simeq 600$ in this study). The total number of computation nodes (N) along one spatial direction is estimated by $N \sim 1.6k^{3/2}/(\epsilon\eta_b) \simeq 0.4R_\lambda^{3/2}Sc^{1/2}$. The total number of time steps is $M = 120k^{3/2}/(\pi\epsilon\eta_b) \simeq 9.2\,R_\lambda^{3/2}Sc^{1/2}$. Thus the total floating-point operations are $N^3M \sim 0.55\,R_\lambda^6Sc^2$ in a box domain with N^3 nodes. Using a computer of 1 gigaflop, the computation time to implement the DNS is thus $T_G \simeq (R_\lambda/70)^6Sc^2$. For the low-$Ri$ case in the present study ($R_\lambda \simeq 100$), $T_G \simeq 4,680,000$ days.

Acknowledgment

The authors would like to thank the anonymous reviewers for their constructive comments.

Disclosure statement

No potential conflict of interest was reported by the authors.

References

[1] Clark PU, Pisias NG, Stocker TF, et al. The role of the thermohaline circulation in abrupt climate change. Nature. 2002;415:863–869.
[2] Danabasoglu G, Large WG, Briegleb BP. Climate impacts of parameterized Nordic Sea overflows. J Geophys Res. 2010;115:C11005.
[3] Zhang Z, Chen X, Mazumdar S, et al. Experimental and numerical investigation of airflow and contaminant transport in an airliner cabin mockup. Build Environ. 2009;44:85–94.
[4] Turner J. Buoyancy effects in fluids. New York (NY): Cambridge University Press; 1973.
[5] Ivey G, Imberger J. On the nature of turbulence in a stratified fluid. Part 1: the energetics of mixing. J Phys Oceanogr. 1991;21:650–658.
[6] Caulfield C, Peltier W. The anatomy of the mixing transition in homogeneous and stratified free shear layers. J Fluid Mech. 2000;413:1–47.
[7] Peltier W, Caulfield CP. Mixing efficiency in stratified shear flows. Ann Rev Fluid Mech. 2003;35:135–167.
[8] Townsend A. The effects of radiative transfer on turbulent flow of a stratified fluid. J Fluid Mech. 1958;4:361–372.
[9] Mellor G, Yamada T. Development of a turbulence closure model for geophysical fluid problems. Rev Geophys Space Phys. 1982;20:851–875.
[10] Nakanish M. Improvement of the Mellor-Yamada turbulence closure model based on Large-Eddy Simulation data. Bound-Lay Meteorol. 2001;99:349–378.
[11] Canuto V, Howard A, Cheng Y, et al. Ocean turbulence. Part I: one-point closure model-momentum and heat vertical diffusivities. J Phys Oceanogr. 2001;31:1413–1426.
[12] Linden P. Mixing across a density interface produced by grid turbulence. J Fluid Mech. 1980;100:691–703.
[13] Mcewan A. Internal mixing in stratified fluids. J Fluid Mech. 1983;128:59–80.
[14] Strang E, Fernando H. Entrainment and mixing in stratified shear flows. J Fluid Mech. 2001;428:349–386.
[15] Pardyjak E, Monti P, Fernando H. Flux Richardson number measurements in stable atmospheric shear flows. J Fluid Mech. 2002;459:307–316.
[16] Lozovatsky I, Roget E, Fernando H, et al. Sheared turbulence in a weakly-stratified upper ocean. Deep-Sea Res I. 2006;53:387–407.
[17] Lozovatsky I, Fernando H. Mixing efficiency in natural flows. Phil Trans R Soc A. 2013;371:20120213:[19 p.].
[18] Elliott Z, Venayagamoorthy S. Evaluation of turbulent Prandtl (Schmidt) number parameterizations for stably stratified environmental flows. Dyn Atmos Oceans. 2011;51:137–150.
[19] Bouffard D, Boegman L. A diapycnal diffusivity model for stratified environmental flows. Dyn Atmos Oceans. 2013;61–62:14–34.
[20] Shih L, Koseff J, Ivey G, et al. Parameterization of turbulent fluxes and scales using homogeneous sheared stably stratified turbulence simulations. J Fluid Mech. 2005;525:193–214.
[21] Barry M, Ivey G, Winters K, et al. Measurements of diapycnal diffusivities in stratified fluids. J Fluid Mech. 2001;442:267–291.
[22] Stretch D, Venayagamoorthy S. Diapycnal diffusivities in homogeneous stratified turbulence. Geophys Res Lett. 2010;37:L02602.
[23] Mater B, Venayagamoorthy S. The quest for an unambiguous parameterization of mixing efficiency in stably stratified geophysical flows. Geophys Res Lett. 2014;41:4646–4653.
[24] Gonzalez-Juez E, Kerstein A, Shih L. Vertical mixing in homogeneous sheared stratified turbulence: a one-dimensional-turbulence study. Phys Fluids. 2011;23:055106.
[25] Venayagamoorthy S, Stretch D. On the turbulent Prandtl number in homogeneous stably stratified turbulence. J Fluid Mech. 2010;644:359–369.
[26] Munk W, Anderson E. Notes on a theory of the thermocline. J Marine Res. 1948;7:276–295.
[27] Peters H, Gregg M, Toole J. On the parameterization of equatorial turbulence. J Geophys Res. 1988;93:1199–1218.

[28] Kim J, Mahrt L. Simple formulation of turbulent mixing in the stable free atmosphere and nocturnal boundary layer. Tellus. 1992;44A:381–394.
[29] Kays W. Turbulent Prandtl number. Where are we? J Heat Trans. 1994;116:284–295.
[30] Price J, Baringer M, Lueck R, et al. Mediterranean Outflow mixing and dynamics. Science. 1993;259:1277–1282.
[31] Girton J, Sanford T, Käse R. Synoptic sections of the denmark strait overflow. Geophys Res Lett. 2001;28:1619–1622.
[32] Baines PG. Mixing regimes for the flow of dense fluid down slopes into stratified environment. J Fluid Mech. 2005;538:245–267.
[33] Thomas P, Linden P. Rotating gravity currents: small-scale and large-scale laboratory experiments and geostrophic model. J Fluid Mech. 2007;578:35–65.
[34] Ivey GN, Winters KB, Koseff JR. Density stratification, turbulence, but how much mixing? Ann Rev Fluid Mech. 2008;40: 169–184.
[35] Dahm WJA, Dimotakis PE. Measurements of entrainment and mixing in turbulent jets. AIAA Journal. 1987;25:1216–1223.
[36] Crimaldi JP, Koseff JR. High-resolution measurements of the spatial and temporal scalar structure of a turbulent plume. Exp Fluids. 2001;31:90–102.
[37] Troy C, Koseff J. The generation and quantitative visualization of breaking internal waves. Exp Fluids. 2005;38:549–562.
[38] Horner-Devine AR. Velocity, density and transport measurements in rotating, stratified flows. Exp Fluids. 2006;41:559–571.
[39] Hult E, Troy C, Koseff J. The breaking of interfacial waves at a submerged bathymetric ridge. J Fluid Mech. 2009;637:45–71.
[40] Odier P, Chen J, Rivera MK, et al. Mixing in stratified gravity currents: Prandtl mixing length. Phys Rev Lett. 2009;102:134504:[4 p.].
[41] Williams PD, Kelsall CW. The dynamics of baroclinic zonal jets. J Atmos Sci. 2015;72:1137–1151.
[42] Pope SB. Turbulent flows. Cambridge: Cambridge University Press; 2001.
[43] Xu D, Chen J. Experimental study of stratified jet by simultaneous measurements of velocity and density fields. Exp Fluids. 2012;53:145–162.
[44] Sheng J, Meng H, Fox RO. A large eddy PIV method for turbulence dissipation rate estimation. Chem Eng Sci. 2000;55:4423–4434.
[45] Tanaka T, Eaton JK. A correction method for measuring turbulence kinetic energy dissipation rate by PIV. Exp Fluids. 2007;42:893–902.
[46] Lavoie P, Avallone G, Gregorio FD, et al. Spatial resolution of PIV for the measurement of turbulence. Exp Fluids. 2007;43:39–51.
[47] Xu D, Chen J. Accurate estimate of turbulent dissipation rate using PIV data. Exp Therm Fluid Sci. 2013;44:662–672.
[48] Doron P, Bertuccioli L, Katz J, et al. Turbulence characteristics and dissipation estimates in the costal ocean bottom boundary layer from PIV data. J Phys Oceanography. 2001;31:2108–2134.
[49] Steinbuck JV, Roberts PLD, Troy CD, et al. An autonomous open-ocean stereoscopic PIV profiler. J Atmos Oceanic Technol. 2010;27:1362–1380.
[50] Raffel M, Willert C, Wereley S, et al. Particle image velocimetry - a practical guide. 2nd ed. Berlin: Springer; 2007.
[51] Batchelor GK. Small-scale variation of convected quantities like temperature in turbulent fluid. Part 1. General discussion and the case of small conductivity. J Fluid Mech. 1959;5:113–133.
[52] Miles JW. On the stability of heterogeneous shear flows. J Fluid Mech. 1961;10:496–508.
[53] Howard LN. Note on a paper by J. W. Miles. J Fluid Mech. 1961;10:509–512.
[54] Abarbanel HD, Holm DD, Marsden JE, et al. Richardson number criterion for the non-linear stability of 3D stratified flow. Phys Rev Lett. 1984;52:2352–2355.
[55] Odier P, Chen J, Ecke R. Entrainment and mixing in a laboratory model of oceanic overflow. J Fluid Mech. 2014;746:498–535.
[56] Armenio V, Sarkar S. An investigation of stably stratified turbulent channel flow using large-eddy simulation. J Fluid Mech. 2002;459:1–42.

[57] Troen IB, Mahrt L. A simple model of the atmospheric boundary layer; sensitivity to surface evaporation. Bound-Lay Meteorol. 1986;37:129–148.
[58] Large WG, McWilliams JC, Doney SC. Oceanic vertical mixing: a review and a model with nonlocal boundary layer parameterization. Rev Geophys. 1994;32:363–403.
[59] Osborn T. Estimates of the local rate of vertical diffusion from dissipation measurements. J Phys Oceanogr. 1980;10:83–89.
[60] MacKinnon J, Gregg M. Near-inertial waves on the New England shelf: the role of evolving stratification, turbulent dissipation, and bottom drag. J Phys Oceanogr. 2005;35:2408–2424.
[61] Venayagamoorthy S, Stretch D. Lagrangian mixing in decaying stably stratified turbulence. J Fluid Mech. 2006;564:197–226.
[62] Stretch DD, Rottman JW, Venayagamoorthy SK, et al. Mixing efficiency in decaying stably stratified turbulence. Dyn Atm Oceans. 2010;49:25–36.
[63] Fernando H. Turbulent mixing in stratified fluids. Ann Rev Fluid Mech. 1991;23:455–493.
[64] Strang EJ, Fernando HJS. Vertical mixing and tranports through a stratified shear layer. J Phys Oceanogr. 2001;31:2026–2048.
[65] Kays W, Crawford M. Convective heat and mass transfter. New York (NY): McGraw-Hill; 1993.